Atmos. Chem. Phys. Discuss., 15, 4383–4426, 2015
www.atmos-chem-phys-discuss.net/15/4383/2015/
doi:10.5194/acpd-15-4383-2015

Atmospheric Chemistry and Physics Discussions

Impact of the 2009 major stratospheric sudden warming on the composition of the stratosphere

M. Tao[1], P. Konopka[1], F. Ploeger[1], J.-U. Grooß[1], R. Müller[1], C. M. Volk[2], K. A. Walker[3], and M. Riese[1]

[1]Forschungszentrum Jülich (IEK-7: Stratosphere), Germany
[2]Department of Physics, University of Wuppertal, Germany
[3]Department of Physics, University of Toronto, Toronto, Ontario, Canada

Received: 11 December 2014 – Accepted: 27 January 2015 – Published: 17 February 2015

Correspondence to: M. Tao (m.tao@fz-juelich.de)

Published by Copernicus Publications on behalf of the European Geosciences Union.

Abstract

In a case study of a remarkable Major stratospheric sudden Warming (MW) during the boreal winter 2008/09, we investigate how transport and mixing triggered by this event affect the composition of the whole stratosphere in the Northern Hemisphere. We simulate this event with the Chemical Lagrangian Model of the Stratosphere (CLaMS), with optimized mixing parameters and with no mixing, i.e. with transport occurring only along the Lagrangian trajectories. The results are investigated by using the tracer–tracer correlation technique and by applying the Transformed Eulerian Mean formalism. The CLaMS simulation of N_2O and O_3 with optimized mixing parameters shows good agreement with the Aura Microwave Limb Sounder (MLS) data. The spatial distribution of mixing intensity in CLaMS correlates fairly well with the Eliassen–Palm flux convergence and illustrates how planetary waves drive mixing. By comparing the simulations with and without mixing, we find that after the MW poleward transport of air increases not only across the vortex edge but also across the subtropical transport barrier. Moreover, the MW event also accelerates polar descent and tropical ascent of the Brewer–Dobson circulation. The accelerated ascent in the tropics and descent at high latitudes firstly occurs in the upper stratosphere and then propagates downward to the lower stratosphere. This downward propagation takes over one month from the potential temperature level of 1000 to 400 K.

1 Introduction

A Major stratospheric sudden Warming (MW) is a dramatic phenomenon with strong wind disturbance and polar temperature rise in the winter stratosphere, associated with transport of air from low to high latitudes (see e.g. Andrews et al., 1987). The mechanism of MWs has been understood as a result of tropospheric waves propagating upwards into the stratosphere and breaking at a certain level (Matsuno, 1971). Planetary-scale waves can be diagnosed by the Eliassen–Palm (EP) flux and its di-

ACPD
15, 4383–4426, 2015

vergence (Eliassen, 1951; Plumb and Bell, 1982). In particular, positive and negative values of the EP flux divergence quantify the acceleration and deceleration of the zonal flow, respectively, driving the Brewer–Dobson (BD) circulation.

During a MW event, strong large-scale planetary waves propagate, break and finally dissipate – a process that occurs almost isentropically, i.e. on levels with a constant potential temperature. In the stratospheric chemical tracer fields, the MW itself is characterized by existence of filamentary structures on a broad range of spatial scales (see e.g. McIntyre and Palmer, 1983; Konopka et al., 2003, 2005; Grooß et al., 2005). However, quantitative understanding of MWs is still not entirely achieved, in particular in terms of coupling between dynamics, transport and chemistry. For example, chemical transport models which do not resolve filamentary structures explicitly or realistically represent the dissipation/mixing processes will not simulate non-linear chemical reactions accurately but may either over- or underestimate reaction rates (Tuck, 1986; Orsolini et al., 1997; Edouard et al., 1996; Konopka et al., 2003).

To improve understanding of MW events, many case studies based on modeling and/or satellite data have been done. Based on the Aura Microwave Limb Sounder (MLS) observations, three MWs in the NH winter 2004, 2006 and 2009 were extensively studied with the result that all these events share the similarity of their profound impact on the composition of the lower stratosphere (Manney et al., 2005, 2008, 2009).The MW in 2009 was the most intensive and prolonged case in the record but this event happened when typical known external factors, e.g. the Quasi-Biennial Oscillation, the Southern Oscillation, the 11 year sunspot cycle, were all unfavorable (Labitzke and Kunze, 2009). Ayarzagüena et al. (2011) and Harada et al. (2010) studied this event from the perspective of tropospheric forcing. Both studies pointed out that the pronounced planetary wave-2 in the stratosphere, which triggers the MW, is associated with a tropospheric ridge over Pacific.

This remarkable stratospheric warming event influenced the distribution of chemical species. The amount of air transported out of the polar vortex into the mid-latitudes was weakest before the MW and the strongest after this event (Manney et al., 2009).

ACPD
15, 4383–4426, 2015

Kuttippurath and Nikulin (2012) diagnosed an increasing trend of occurrence of the NH MWs in the recent 10 years (1999–2011). They confirmed the weak chlorine-induced ozone loss due to early onset of MWs during these winters (mainly in December or January). Sofieva et al. (2012) used Global Ozone Monitoring by Occultation of Stars (GOMOS) satellite measurements to study the O_3, NO_2 and NO_3 distribution during the MW and found that changes in composition can extend into the mesosphere and even into the lower thermosphere.

Atmospheric transport can be divided into advection describing transport of an air parcel along the 3d trajectory and mixing parametrizing the small-scale turbulence between the air parcels. Compared with Eulerian transport models with an implicit numerical diffusion, Lagrangian transport models have advantages in separating mixing and thus explicitly describing the mixing process in the atmosphere. In this study, we use the Chemical Lagrangian Model of the Stratosphere (CLaMS), which is based on Lagrangian transport and parametrized mixing along the trajectory by adaptive re-gridding after every 24 h time step (McKenna et al., 2002b). The mixing scheme in CLaMS is based on the concept that large-scale deformations, caused e.g. by wave breaking, are associated with small-scale mixing (Konopka et al., 2004, 2007). Advection in CLaMS is driven by the European Centre for Medium-range Weather Forecast (ECMWF) ERA-Interim reanalysis winds and diabatic heating rates (Dee et al., 2011; Ploeger et al., 2010).

Representation of mixing in the models is the main difficulty in quantifying the permeability of transport barriers like the polar vortex edge or the tropical pipe (Tuck, 1986; Plumb, 1996; Steinhorst et al., 2005; Hoppe et al., 2014). Mixing itself is an irreversible process that occurs on a molecular scale. In a stable stratified stratosphere mixing is mainly driven by isentropic stirring, which is associated with large-scale wave breaking and wind shear (McIntyre and Palmer, 1983). Riese et al. (2012) assessed the influence of uncertainties in the atmospheric mixing strength on the global distribution of the greenhouse gases (H_2O, O_3, CH_4, N_2O) in the upper troposphere lower stratosphere (UTLS) and on the associated radiative effects. Their results show that simulated ra-

ACPD
15, 4383–4426, 2015

diative effects of H_2O and O_3, both characterized by steep gradients in the UTLS, are particularly sensitive to the atmospheric mixing strength.

To separate and quantify the impact of mixing on transport and chemistry of stratospheric constituents during a MW, we utilize non-linear tracer–tracer correlations. Chemical constituents whose chemical sources and sinks are slow compared with dynamical timescales, are influenced by the Brewer–Dobson circulation and by quasi-isentropic mixing (which is most efficient within the extratopical surf zone) and show compact tracer–tracer relations (Plumb, 2007). Mixing is suppressed at the transport barriers at the edge of the winter polar vortex and at the edges of the tropics, so that tracer relationships distinct from those of middle latitudes occur in the tropics (Volk et al., 1996) and in the polar vortices (e.g., Plumb, 1996; Müller et al., 1996, 2001). Here, we focus on the relationship of O_3 with the long-lived tracer N_2O. Because chemical production and loss terms of O_3 increase strongly with altitude in the stratosphere, ozone can not be considered long-lived at altitudes above ≈ 20 km and relations with N_2O are not necessarily compact (Hegglin and Shepherd, 2007). However, as we will also show below, the transport barriers in the stratosphere are sufficiently strong to allow distinct O_3-N_2O relationships to develop in the polar vortex, the mid latitudes and in the tropics.

The motivation of this work is to improve our understanding of transport and its impact on chemistry in a stratosphere under strongly disturbed dynamical conditions. In particular, the 2009 MW is an excellent case for studying: (1) the multi-scale (days to months) responses to the wave forcing, (2) the evolution of mixing and its effect on distribution of chemical compositions, (3) the interpretation of the observed tracer–tracer correlations using CLaMS simulations. In Sect. 2, we will overview the dynamical background of the stratospheric winter 2008/09. The CLaMS setup and validation with the MLS observations of N_2O and O_3 will be presented in Sect. 3. Section 4 will discuss the simulated mixing intensity in relation to wave forcing. Finally, Sect. 5 will present the N_2O-O_3 correlations and their interpretation in terms of mixing, transport and chem-

ACPD
15, 4383–4426, 2015

istry caused by the MW in January 2009. At last, the main results will be concluded in Sect. 6.

2 Dynamical background

The polar temperature gradient from the North Pole to 60° N at 10 hPa turned to negative in late December of 2008, which meets the minor stratospheric warming criterion of the World Meteorological Organization (WMO). The onset of the MW was January 24th. According to the WMO criteria (McInturff, 1978; Andrews et al., 1987; Charlton and Polvani, 2007), both 60° N zonal wind and polar temperature gradient at 10 hPa reversed at this day. Here we use January 23 as the central day of MW because the polar cap temperature reached its peak on January 23 instead of 24th.

Figure 1a shows that the sudden rise of polar cap temperature started in the upper stratosphere, around January 10 at 1 hPa, then the warming propagated downward, arriving at 10 hPa and descended to the lower stratosphere until late January. The increase of polar temperature was accompanied by generation of easterlies, which are also shown in Fig. 1a (black contours). The easterlies and temperature rise lasted only 10 days at 1 hPa followed by a strong polar vortex cooling while disturbance of wind and temperature in the lower stratosphere lasted more than 1 month without a complete recovery until the final warming in the spring of 2009.

Relative to the long-term average, the lower stratosphere in the tropics was slightly warmer before the MW due to the westerly phase of the QBO in this winter. Similar to the warming in the high latitudes, the tropical cooling (Fig. 1b) also started at about 15 January at 1 hPa and descended from the upper to the lower stratosphere during 2 weeks. As discussed in Randel et al. (2002), time-dependent upwelling in the tropical lower stratosphere is correlated with transient extratropical planetary waves which transport heat from the tropics to high latitudes and, at the end, drive the BD-circulation.

A widely used diagnostic of the upward-propagating waves is the vertical component of the EP flux, for which the strongest contribution results from the horizontal eddy

ACPD
15, 4383–4426, 2015

heat flux $\overline{v'T'}$ with $v' = v - \overline{v}$, $T' = T - \overline{T}$ and with overbar denoting zonal mean and primes describing the deviations (i.e. fluctuations) for the temperature T and for the meridional velocity v (Andrews et al., 1987; Newman et al., 2001). Figure 1c shows the time evolution of the eddy heat flux at 100 hPa averaged between 40 and 70° N which explains more than 80 % of the variability of the total vertical component of the EP flux. In addition, contributions of the wave-1 and wave-2 components to the mean eddy heat flux are also shown.

Newman et al. (2001) pointed out that the eddy heat flux measures activity of the waves and is highly correlated with the time evolution of the stratospheric polar temperature. As can be deduced from Fig. 1e and a (or b), the mean eddy heat flux at 100 hPa was well correlated with warming at the North Pole and cooling in the tropics. It shows a $1 \sim 2$ weeks oscillation ranging within 0–25 $\mathrm{m\,K^{-1}\,s^{-1}}$ in December and it began to increase from 6 January reaching the first peak on 18 January. After several days of a slight decay, it rose up to the second peak on 27 January and then gradually declined to 0 around mid-February with some small fluctuations afterwards. The dominant wave number before and during the MW was wave-2, which led to the vortex split. However, after the MW, the main contribution to the total eddy heat flux resulted from higher wave numbers.

Large-scale tropospheric waves can propagate upward into the stratosphere through weak westerlies and break at the critical level, disturbing the mean flow (Dickinson, 1968; Matsuno, 1971). Such a transient wave breaking converts the zonal flow momentum to mean meridional circulation, and thus drives the extra-tropical downwelling and tropical upwelling of the BD circulation.The temperature perturbations discussed above and shown in Fig. 1a and b result directly from adiabatic heating and cooling caused by these wave-driven vertical motions. Subsequently, temperatures gradually relax toward their radiative equilibrium values by additional radiative cooling or heating, amounting to additional diabatic motion, i.e. down- or upwelling through isentropic surfaces. The polar and tropical heating rate anomalies from the 24 year mean of ECMWF meteorological ERA-Interim reanalysis (Dee et al., 2011) are shown in Fig. 1d and e. As

ACPD
15, 4383–4426, 2015

expected, diabatic polar downwelling and tropical upwelling (quantified by these heating rates) were both accelerated after the onset of the MW. As also expected, the onset of the heating rate anomalies at each altitude, and thus their downward propagation, is roughly synchronous with the temperature anomalies shown in Fig. 1a and b. The radiative decay of the anomalies takes only about 10 days at 1000 K, but more than one month below 500 K. This is consistent with the stratospheric radiative relaxation time inferred from satellite measurements (Mlynczak et al., 1999), which was found to increase from 10 days at 1 hPa to about 100 days at 50 hPa.

3 Model description and validation

3.1 Model setup

CLaMS is a Lagrangian chemistry transport model with mixing that can be switched off, so that the transport is carried out only along 3d forward trajectories. However, a pure Lagrangian transport approach gives rise to many unrealistic small-scale structures due to lack of mixing (Konopka et al., 2004; Khosrawi et al., 2005). Hence, irreversible small-scale mixing between air parcels (APs) should be considered. With the concept that (small-scale) mixing is driven by large-scale flow deformation, the CLaMS mixing procedure is realized through the adaptive re-gridding of the irregular grid. More specifically, the APs are inserted or merged when the distances between the next neighbors increase above or decrease below a critical distance. The critical deformation γ_c is defined as $\gamma_c = \lambda_c \Delta t$ with the critical Lyapunov exponent λ_c and the advective time step Δt which are set to 1.5 day^{-1} and 24 h, respectively (for more details see McKenna et al., 2002b; Konopka et al., 2004).

CLaMS simulations cover the 2008/09 boreal winter from 1 December 2008 to 1 April 2009 and extend between the Earth's surface and the potential temperature θ = 2500 K (i.e. rougly around the stratopause with $p \approx 0.3$ hPa). The horizontal separation of the APs initialized on December 1 is 70 km in the NH, where all our results are obtained,

ACPD
15, 4383–4426, 2015

and 200 km in the SH. During the course of the simulation, this irregular grid of APs undergoes advection along the trajectories, chemistry and mixing every time step Δt = 24 hours as described in Konopka et al. (2004); Grooß et al. (2005); Pommrich et al. (2014).

The horizontal winds are prescribed by the ECMWF ERA-Interim reanalysis (Dee et al., 2011). In the stratosphere, the potential temperature θ is employed as the vertical coordinate of the model and the cross-isentropic velocity $\dot{\theta} = Q$ is deduced from the ERA-Interim forecast total diabatic heating rates Q, including the effects of all-sky radiative heating, latent heat release and diffusive heating as described by Ploeger et al. (2010). The time evolution of the anomaly of $\dot{\theta}$ averaged over the polar cap and over the tropics is shown in Fig. 1c, d and was discussed in the previous section.

N_2O and O_3, the most important species on this work, are initialized from the MLS data (more details on MLS can be found in the next subsection). The other chemical species are initialized from a multi-annual CLaMS simulation (Pommrich et al., 2014). At the upper boundary (2500 K) O_3 is set to the HALOE climatology after every 24 h time step. However, the impact of the upper boundary condition on the chemical tracers is not significant below 1000 K. The chemistry module of CLaMS is described in McKenna et al. (2002a).

The simulation includes ozone (O_3) calculated with full chemistry and passively transported O_3 without any chemistry (pO_3). By switching off and on the mixing module, we get two additional sets of simulations: full chemistry without mixing and full chemistry with mixing being our reference as the best model representation of the real atmosphere.

3.2 Validation with the MLS observations

MLS observes microwave emission from the limb of the Earth's atmosphere in the direction of the Aura orbit. The instrument measures vertical profiles from the troposphere to the mesosphere every 165 km (1.5° along the Aura orbit), providing about 3500 profiles per day. We use version 3.3 N_2O and O_3 from the MLS product (Livesey

ACPD
15, 4383–4426, 2015

et al., 2011) both to initialize and to validate the CLaMS reference simulation. The vertical resolution of O_3 is about 2.5–3 km in the stratosphere with a 5–10 % uncertainty (Livesey et al., 2011, 2013). The vertical resolution of N_2O is about 4–6 km with a 9–25 % uncertainty for the region of interest in this study (Livesey et al., 2011). Averaging kernels are applied in the retrieval of the MLS profiles, which relate the retrieved MLS profiles to the true atmospheric state. More details about MLS v3.3 measurements, data validation and processing algorithms are available at http://mls.jpl.nasa.gov/data/v3-3_data_quality_document.pdf.

For comparison, we map CLaMS mixing ratios to the observed MLS profiles using a back and forward trajectory technique (Ploeger et al., 2013) and apply the MLS averaging kernels to CLaMS output in order to get comparable quantities (see Appendix). Because CLaMS APs are saved every day only at 12:00 UTC, we calculate the noon-positions of the MLS observations within 1 day window using back and forward trajectories, and then select the nearest CLaMS AP to the corresponding MLS observation. The mixing ratios at this AP are then compared with the respective MLS observations.

Hereby, a one-to-one MLS-CLaMS data set for N_2O and O_3 is established that is plotted in Fig. 2 as probability distribution functions (PDFs) calculated for the whole NH and for the entire simulation period. According to a high correlation coefficient both for N_2O and for O_3, our reference simulation matches the MLS observations fairly well.

For a further comparison, we investigate the horizontal distribution of N_2O. Figure 3 shows the comparison between the CLaMS simulation and MLS observations for five selected days at θ = 800 K (top 2 panels) and 475 K (bottom 2 panels). On 9 January, the vortex was centered around the North Pole and the vortex structure was very stable. Influenced by the planetary wave-2, the polar vortex stretched to North America and Asia on both heights during the following days. Around the central day of MW at 23 January, a double center structure formed which split up until 25 January at 475 K and until 28 January at 475 K (not shown).

In the following days, an increasing number of filaments could be observed outside of the vortex which are marked by low N_2O values. The two vortex centers slowly ro-

ACPD
15, 4383–4426, 2015

tated anticlockwise. One of the vortex remnants over Eastern America and the Atlantic stretched further, split and dissolved releasing its content to mid-latitudes, while another one stayed over northern Asia and the Pacific Ocean. Although in the following weeks most of the vortex fragments were largely mixed with mid-latitude air, part of them, like those over northern Asia and the Pacific Ocean, re-organized as a new and relatively weak vortex. However, this top-down process that started in late February at 800 K (a weak, circumpolar vortex edge can be diagnosed at θ = 800 K at 20 February, see Fig. 3) and was finished in mid March at 475 K (not shown) is excluded from our analysis that ends on 28 February.

The distribution of simulated N_2O accurately represents the MLS observations although more filamentary structures are resolved in CLaMS simulations. It should be noted that applying averaging kernels to model result also smoothes some valuable information, e.g. filamentary structures, and, consequently, may result in a misinterpretation of the stratospheric composition, especially for high-latitude N_2O. More details are discussed in the Appendix.

4 Planetary waves and mixing

4.1 Transport and mixing barriers in the winter hemisphere

In the winter overworld stratosphere, there are two main barriers denoted as two thick blue lines in Fig. 4 (Holton et al., 1995). One is the polar vortex edge defined by a peak of westerlies and identified as the maximum gradient of potential vorticity (PV) with respect to equivalent latitude (in the following eq. latitude, Nash et al., 1996). The second barrier (around 10–30° N eq. latitude which varies with altitudes) separates the surf zone (McIntyre and Palmer, 1983) from the region of tropical upwelling, the so-called tropical pipe (Plumb, 1996).

This subtropical barrier is not as well-defined as the polar vortex edge and is usually characterized by a much weaker PV gradient between tropics and mid-latitudes

ACPD
15, 4383–4426, 2015

(Polvani et al., 1995) although large meridional tracer gradients can be diagnosed (Punge et al., 2009). While the polar vortex edge is considered as a meridional transport barrier due to a strong polar jet, the subtropical barrier is only weakly influenced by the jets and is usually understood as a barrier for eddy mixing. This barrier is strongly related to the phase of the Quasi-Biennial Oscillation (QBO): during the westerly QBO, planetary waves generated in the winter hemisphere can propagate across the equator to dissipate at the summer hemisphere easterlies whereas such propagation is suppressed during the easterly QBO phase (Haynes and Shuckburgh, 2000; Shuckburgh et al., 2001; Punge et al., 2009). Thus, during the 2008/09 winter, the subtropical transport barrier was weakened by the westerly QBO phase (dashed thick blue line in Fig. 4).

In a winter with weak activity of planetary waves, the exchange and mixing of air across the vortex edge is suppressed. However, once a sudden warming event happens, the enhanced wave forcing drives significant isentropic, two-way mixing (red curved arrows) as well as the large-scale BD circulation (gray arrows). The evolution of the dynamical fields, including cross-isentropic vertical velocity $\dot{\theta}$ and zonal wind, was discussed in the previous section (Fig. 1). But isentropic mixing and its relation to wave forcing need further investigations.

4.2 CLaMS mixing vs. wave forcing

Mixing between the Lagrangian APs is parametrized in CLaMS through adaptive regridding. During this process, the involved APs (i.e. APs, which were generated by the mixing algorithm), are marked after every 24 h time-step. Here we use the statistics of these events, i.e. the percentage of mixed APs relative to all transported APs, in the following denoted as mixing intensity. In this way, we illustrate the impact of the MW on the distribution and evolution of mixing resolved by the model.

Figure 5 shows the time evolution of the zonally averaged mixing intensity derived from CLaMS vs. eq. latitude. Complementary, Fig. 6 illustrate the relationship between the EP flux divergence and the CLaMS mixing intensity averaged over several stages

ACPD
15, 4383–4426, 2015

of the polar vortex during the winter 2008/09: (a) stable vertex conditions in January between 3 and 13, (b) 10 days period before the MW, i.e. between 14 and 23 January, (c) 10 days period after the MW, i.e. between 24 January and 3 February, and (d) stable stratospheric conditions after the MW between 4 and 13 February.

We notice that before mid January maximum mixing remains equatorward of 65° N and generally outside the polar vortex boundary as defined by the Nash criterion. In particular above 700 K the rather abrupt poleward decrease in mixing strength clearly marks the polar mixing barrier isolating the core of the stable polar vortex from the surf zone. Note that the Nash criterion is not necessarily a perfect proxy for the mixing barrier, thus mismatch to within a few degrees latitude, as apparent in Fig. 5a, is not surprising. In mid-January the picture changes drastically. With the intensified wave activity disturbing the polar vortex, the westerlies decelerated. Consequently, the EP flux increased and its divergence became strongly negative meaning an enhanced convergence of the EP-flux. Furthermore, the pattern of mixing intensity separated into two branches above 700 K after 24 January: one in high and another one in mid eq. latitudes (marked as A1 and A2 in Figs. 5a and 6c, respectively).

This distribution of mixing intensity indicates that both the polar and subtropical barrier (the latter above 700 K) are weakened by the MW. Furthermore, daily PV or tracer distributions over the NH (cf. Fig. 3) exhibit that at this time several vortex fragments move equatorward and mix with mid-latitude air. At the same time, several fragments of tropical air masses which are generated at low latitudes, transport polewards and mix with mid- or high latitude air.

Mixing intensity diagnosed in Fig. 5 shows some interesting, altitude-dependent patterns: at the highest levels (θ between 700 and 850 K) and after the MW, the mid- and high-latitude mixing is comparable (cf. A1 vs. A2 in Fig. 5a). At the levels between 500 and 700 K, the high-latitude mixing branch within the vortex dominates. Finally, in the lower stratosphere between 400 and 500 K, mixing has intensified in the pole region after the MW while the mixing intensity in the surf zone (marked as B in Fig. 5c) has slightly but not significantly enhanced during and after the MW. Note that the subtrop-

ACPD
15, 4383–4426, 2015

ical barrier can be identified as a minimum in mixing intensity between 10 and 20° N eq. latitude (Fig. 5b). The position of this minimum does not significantly change during the time although the impact of the MW can be seen around 1 February, mainly at highest levels between 700 and 850 K.

From the vertical cross sections shown in Fig. 6, we infer that in the first half of January, there were 3 intensive mixing regions (marked as A, B and C) with only weak, vertically propagating waves. As mentioned above, region A became stronger during the course of the winter and then divided into two branches (A1 and A2). Region B is related to the mid-latitude (surf zone) mixing in the lower stratosphere (400–500 K) that is influenced by the subtropical jet and the QBO. Region C is associated with strong vertical shear in the transition layer between the westerlies and easterlies of the QBO.

It is obvious that although before the MW high mixing intensities can be diagnosed in the surf zone outside of the polar vortex (region A), this signature intensifies after the onset of the MW (regions A1 and A2). Convergence of the EP flux indicates breaking of waves and thus leads to wave-mean-flow interaction. Once the local wind field is significantly disturbed by transport of momentum and heat flux, subsequent stirring and stretching of eddies (resolved by the ECMWF winds) drives the mixing parametrization in CLaMS. Note that after 10 February (20 days after MW), the mixing intensity quickly dropped as the vortex started to recover with a weak vortex edge between 50 and 60° N eq. latitude at 800 K and 50° N eq. latitude at 600 K (i.e. with a weak PV gradient according to the Nash criterion).

Based on the analysis of the temporal and spatial evolution of the mixing intensity resolved in CLaMS and the EP flux divergence, the simulated patterns show a clear and reasonable physical picture how mixing does respond to large-scale wave forcing: when the general circulation is strong and stable, the mixing pattern is also stable; when the general circulation is disturbed and weakened by the large-scale wave forcing, the pattern of mixing is largely determined by the local wave activities. However, the question still arises if mixing resolved by the model can also be seen in the observations, e.g. in a change of the N_2O-O_3 correlations measured by the MLS instrument. Another

ACPD
15, 4383–4426, 2015

important point is a more quantitative understanding how the MW itself influences the chemical composition of the stratosphere.

5 Impact of the MW on transport and chemistry

5.1 N_2O-O_3 correlations

As discussed in the last section, the subtropical barrier and much more the polar vortex barrier suppress the exchange of APs across those barriers before the MW. Hence, long-lived species are well-mixed in the regions segregated by these barriers and strong isentropic gradients of these species are expected across such barriers. Using the tracer–tracer correlation technique (for a review of this method see Plumb, 2007), the well-mixed regions manifest as compact correlations which are well-separated in the tracer–tracer space.

Figure 7 shows the N_2O-O_3 correlation of the MLS observations plotted as a probability distribution functions (PDFs) due to the large number of observations (around 10 thousand points). The data covers the NH with eq. latitudes between 0 and 90° N and within the potential temperature range between 450 and 700 K. The MLS observations are selected for three periods: 18–28 December (one month before the MW), 18–28 January (during the MW); 18–28 February (one month after the MW). The gray lines in Fig. 7 indicate the isentropes calculated from the observed pressure altitude and corresponding ECMWF temperature.

Under relatively stable dynamical conditions before the MW, two stronger and one weaker N_2O-O_3 correlation branches with enhanced PDF values can be distinguished in Fig. 7a which describe the well-mixed air masses within the polar vortex, within the surf zone and within the tropics (thin black lines from bottom to the top, respectively). The corresponding barriers in the physical space (see Fig. 4), i.e. the vortex edge and the subtropical barrier, manifest in the tracer–tracer space as regions with lower PDF values separating the correlation lines. After the MW (see Fig. 7c), the polar N_2O-O_3

ACPD
15, 4383–4426, 2015

correlation totally disappears in the tracer–tracer space and the tropical correlation becomes slightly weaker. Reversely, the PDF of the mid-latitude N_2O-O_3 correlation strengthens at the same time.

Before a general picture of transport and chemistry triggered by the MW in January 2009 will be discussed in the following two subsections, Fig. 8 shows schematically how these processes can be separated by using the N_2O-O_3 correlations. Here, three idealized correlation lines for the polar vortex, surf zone and tropics are plotted which are crossed by two isentropes with θ = 500 and 700 K. Thus, through isentropic mixing, the APs in the mid-latitudes change their composition as they mix with other APs isentropically transported from higher or lower latitudes. Consequently, mixing lines connecting the isolated correlations may appear or, when an intensive and persistent mixing happens, the whole correlation line inclines to one side.

Reversely, if the APs are affected by a strong vertical transport like cross-isentropic motion due to wave forcing commonly denoted as up- or downwelling, the composition of the APs stays roughly the same although their θ-coordinate significantly changes. In other words, an AP will not change its coordinates in the tracer–tracer space although it will move in physical space. In the N_2O-O_3 space, this type of motion manifests in the change of the position relative to the isentropes which are different before and after the MW (from solid to dashed in Fig. 8).

Furthermore, if only APs within a limited range of the potential temperature are selected, the cross-isentropic transport results in an additional flux of the APs out of (export) or into (import) the considered domain and, consequently, the N_2O-O_3 correlation will change. In the same way, export or import of APs from a limited range of eq. latitudes influences the N_2O-O_3 correlation (e.g. if the subtropical barrier moves toward the equator).

Finally, chemistry can also influence the N_2O-O_3 correlations. Because the N_2O production and loss can be neglected on the considered time-scales, only the O_3 chemistry can change the particular branches of the N_2O-O_3 correlations. Particularly, increasing halogen or NO_x-induced ozone loss would shift the polar or the surf zone cor-

ACPD
15, 4383–4426, 2015

relations downwards whereas increasing ozone production in the low latitudes would make the tropical or the surf zone correlations steeper.

5.2 Isentropic mixing vs. cross-isentropic transport

Our first goal is to understand the changes in the N_2O-O_3 correlations observed by the MLS before and after the MW (Fig. 7a–c) as a result of different transport mechanisms (isentropic mixing, diabatic descent, meridional transport) or/and as the effect of ozone chemistry. In particular, we would like to figure out why the polar and the tropical N_2O-O_3 correlations weakened after the MW and the mid-latitude correlation becomes stronger. First, we rule out the ozone chemistry by using CLaMS simulations with passively transported O_3 (pO_3). In the next subsection, we will also include CLaMS results with the full stratospheric ozone chemistry.

Thus, two sets of CLaMS simulations, with and without mixing, are used to study the mixing-induced differences between the PDFs of the pO_3-N_2O correlations in Fig. 9 (top and bottom row for simulation with and without mixing, respectively). Similar as in Fig. 7, the PDFs are calculated for the same time periods before during and after the MW (from a to c). However, the range of the considered eq. latitudes is confined to 40–90° N (instead of 0–90° N shown in Fig. 7).

Using this limited range of eq. latitudes we exclude the APs on the tropical side of the subtropical barrier (that is around 20° N eq. latitude) and, consequently, the PDFs of the CLaMS run with mixing (upper row of Fig. 9) do not show the tropical correlation (solid dashed line). However, this correlation can be found in the non-mixing run during and after the MW (Fig. 9b2 and c2).

This indicates that the tropical APs transported from lower latitudes, mix with the mid-latitude APs and, consequently, the slope of the surf-zone correlation moves towards the tropical correlation, especially between 550 to 650 K. This isentropic mixing is also consistent with the increased mixing intensity marked as A2 in Figs. 5 and 6. An idealized, pure trajectory calculation (i.e. CLaMS without mixing) completely ne-

ACPD
15, 4383–4426, 2015

glects this effect and produces N_2O-O_3 correlations which cannot be reconciled with observations.

Furthermore, all APs which are transported along the trajactories without mixing do not change their composition and keep the same position in the N_2O-O_3 space unless they leave the considered range of eq. latitudes or potential temperatures. Besides the almost isentropic import of tropical APs that was mentioned in the last paragraph, the strong downwelling within the polar vortex, mainly during the MW itself, can also be diagnosed in the N_2O-O_3 space. First the isentropes calculated from the APs without mixing move upwards (from Fig. 9b2 to c2), as a consequence of diabatic cooling (downwelling) associated with warming in the mid- and high latitudes (see also Fig. 8). As a consequence of this cross-isentropic transport, the APs transported without mixing may be exported (or imported) from (or into) the considered θ-range between 450 and 700 K. In particular such missing polar APs are obvious within the black solid squares in Fig. 9a2 to c2 defined by the N_2O values between 80–130 ppbv and O_3 between 2.7–3.5 ppmv.

In Fig. 10 we plot the eq. latitudes and the potential temperature coordinates of these missing APs at the end of each of the considered time periods (from the CLaMS run without mixing). Furthermore, the APs are colored by different ranges of pO_3 and the PDFs of their eq. latitudes and θ coordinates describe their mean horizontal and vertical position during the course of the winter.

Figure 10 shows that after the MW, most of the APs which were originally located above 450 K, have been transported downwards below 450 K. Therefore, the downward cross-isentropic transport within the vortex (diabatic descent) with subsequent export of the APs out of the considered potential temperature range 450–700 K is the main reason for the missing correlation inside the square of Fig. 9c2. Moreover, most of the APs were confined inside the polar vortex before the MW, while after the MW these APs were spread almost uniformly between 40 and 90° N eq. latitude (Fig. 10c) due to chaotic advection after a complete breakup of the two vortices (see Fig. 3 at 475 K).

ACPD
15, 4383–4426, 2015

In the CLaMS run with mixing, the situation is very similar as long as the edge of the stable vortex presents an effective mixing barrier (Fig. 9a1). Later, during the MW, descent and chaotic advection have the same effect as above, i.e. part of the APs carrying the signature of the polar correlation are again eventually exported from the considered theta-range as they descend below 450 K. However, increased mixing between these descending polar APs with the APs outside the vortex, have two additional effects: (i) the signature of the polar correlation is spread to midlatitude APs that do not undergo further descent, such that the signature remains visible in the considered theta range (even for N_2O values 80–130 ppb), and (ii) the mixing with midlatitude (and even tropical) APs causes the polar correlation branch to become less compact and shift toward the midlatitude correlation branch (along the plotted isentropes). Both these effects can be well discerned by comparing Figs. 9b1 and 9b2. Finally, after the breakup of the two vortices, spreading of the polar APs across the hemisphere along with intense mixing with (by far more) midlatidude and tropical APs leads to an almost complete loss of the polar correlation branch (Fig. 9c1), which remains preserved only in few unmixed vortex remnants. As explained by the theory of Plumb (2007), the fast and nearly hemisphere-wide isentropic mixing (as promoted by the MW) results in a single compact extratropical correlation. Futhermore, the large mass of tropical air transported and then mixed into the extratropics after the MW results in a slight shift of that extratropical correlation toward the tropical correlation branch, which is apparent when comparing Fig. 9c1 with a1 (or with c2).

Note that the weak polar correlation in Fig. 9c1 is not resolved in the MLS observations. A potential explanation is a limited spatial resolution of the MLS instrument with vertical resolution of 4–6 km for N_2O and 2.5–3 km for O_3, respectively, and horizontal resolution of 200 km for both species. That means that physical structures below these values are smoothed out by the MLS instrument (an effect sometimes called optical mixing, see Appendix).

ACPD
15, 4383–4426, 2015

5.3 Impact of chemistry

It is generally accepted that polar O_3 loss triggered by halogens mainly occurs in late winter and spring within a sufficiently cold polar vortex and that the NO_x-induced O_3 chemistry roughly follows the halogen chemistry after the vortex breakup with highest values occurring in the middle and lower stratosphere. Because of a relatively warm winter 2008/09 only few PSCs were formed and, consequently, the subsequent, chlorine-induced ozone-loss within the polar vortex was very limited (Kuttippurath and Nikulin, 2012). This can also be inferred from the MLS observations with no significant change of the polar correlation (cf. Fig. 7a and b) as well as from the CLaMS-based correlation with pO_3 that is very close to the correlation observed by the MLS instrument (cf. Fig. 9b1 with Fig. 7b).

However, the O_3 chemistry, plays an important role in our interpretation of the N_2O-O_3 correlations on a seasonal timescale. Especially, when the temperature rises after the MW, the chemical reactions are accelerated. To quantify the chemical effect on the N_2O-O_3 correlation, Fig. 11 shows the pO_3-N_2O correlation within 0–90° N and 450–700 K range overlaid with the correlations from the full chemistry run (dashed curves). From Figure 11 it is evident that the chemistry alters the ozone mixing ratio.

Two regions (marked in Fig. 11 as A and B) of this correlation plot have been investigated in more detail to investigate the chemical change of ozone. Region (A) has N_2O mixing ratios near 140 ppbv and passive ozone near 7400 ppbv on 23 January, corresponding to the most probable latitude of 35° N and 650 K. It is evident that here the chemistry causes ozone depletion. From the locations of 120 air parcels in this area, back-trajectories were calculated for one month along which the chemistry was calculated using the CLaMS chemistry module and additional output to analyze ozone depletion processes in detail similarly as by Crutzen et al. (1995). The average ozone production over this month through oxygen photolysis was 850 ppbv which was outweighed by ozone loss of 1450 ppbv, of which about half could be attributed to NO_x-

ACPD
15, 4383–4426, 2015

catalyzed ozone loss cycles and the remaining other half equally distributed to HO_x, ClO_x and O_x cycles.

Contrary, region (B) with N_2O mixing ratios of 260 ppbv and passive ozone mixing ratios of 3800 ppbv corresponds to most probable latitudes of 11° N and 575 K. Here, the chemistry causes an ozone increase. A similar chemistry simulation along 132 one-month back-trajectories showed an ozone production through oxygen photolysis of 800 ppbv and net ozone depletion by 260 ppbv. Therefore ozone production dominates here. Since gas-phase chemical reactions are temperature-dependent, it was investigated, if the temperature anomaly (see Fig. 1b) has a significant effect on ozone. An identical run along the 132 trajectories, however with temperatures set 3 K higher, did increase the ozone loss by 30 ppbv. The ozone production is not temperature-dependent. An ozone loss rate of 1 ppbv day^{-1} is negligible compared to the changes caused by dynamics that are discussed here. Complementary to our discussion above, we find that in polar latitudes the differences between correlations with or without chemistry are negligible indicating minor importance of the chlorine-induced ozone-loss during this winter.

6 Conclusions

A remarkable MW in January 2009 led to strongly disturbed stratospheric dynamics which manifested in an accelerated polar descent and tropical upwelling. During the following two weeks up to the end of January, this transient signal of cross-isentropic transport propagated down from around 1 to 100 hPa. The radiative relaxation of this anomaly in diabatic heating was relatively fast (10 days) in the upper stratosphere, but took more than a month in the lower stratosphere, there resulting in accelerated polar descent and accelerated tropical upwelling up to late March (Fig. 1).

Associated with the disturbed dynamical background during the MW, strong variability of the chemical species was observed by the MLS instrument. We used CLaMS to simulate transport, mixing and chemistry to interpret the change of the strato-

ACPD
15, 4383–4426, 2015

spheric composition. By comparison with MLS observations of N_2O-O_3 correlations, we showed how the polar vortex edge weakened and how the subtropical mixing barrier was affected by poleward transport followed by mixing in mid-latitudes during and after the MW.

As an important but uncertain piece of atmospheric modeling, the mixing process could be explicitly and reasonably described in CLaMS simulations. The distribution of simulated mixing intensity showed that mixing across the vortex edge and (above 700 K) also across the subtropical barrier was enhanced after the onset of the MW and were triggered by wave forcing quantified in terms of the EP flux divergence.

The O_3-N_2O correlations have shown to be a useful diagnostic to separate dynamical and chemical effects. Model results show isentropic mixing is a key process to understand the drastic change of stratospheric composition triggered by the MW: the decay of the polar O_3-N_2O correlation and the strengthening of the mid-latitude correlation. One month after the MW, almost half of the vortex dissolved due to isentropic mixing, whereas the other part was a germ of a new and relatively weak vortex. Although the halogen-induced ozone loss within the polar vortex was negligible during this winter, the dominant ozone chemistry during and after the MW was the extra-tropical ozone loss due to NO_x and ozone production in the tropics.

However, there is also a limitation of the applicability of the MLS satellite data with vertical resolution of the order of few kilometers. As shown in the appendix, due to this limited spatial resolution, physical structures below these values and resolved by the model are smoothed out by the satellite's averaging kernel (an effect sometimes called optical mixing). Thus, although MLS satellite data offer a very good coverage, their poor vertical resolution does not allow to narrow the possible range of the mixing parameters in CLaMS (i.e. of the Lyapunov exponent).

Finally, we can speculate that for a winter with a significant, chlorine-induced ozone loss followed by a strong MW the mid-latitude air can be influenced by processed, ozone-depleted air. Conversely, O_3-rich air can be effectively transported into the high latitudes.

ACPD
15, 4383–4426, 2015

Appendix A:

As discussed in Sect. 3.2, the MLS averaging kernels were applied for both the N_2O and O_3 CLaMS output before comparing these distributions with the satellite-based observations. Given a "true" atmospheric profile x_i on n pressure levels $i = 1, \ldots, n$, the averaging kernel can be understood as a smoothing procedure that determines mixing ratios at each level i by a weighted integration over all other levels with a strongest contribution of levels directly above or below the considered level i. The averaging kernel is a matrix A_{ij} with most significant terms around the diagonal and with all rows i fulfilling the normalization condition $\sum_{j=1,\ldots,n} A_{ij} = 1$. Thus, applying averaging kernels to model data with a high spatial resolution like CLaMS means smoothing or removing small-scale structure from the model.

In Fig. 12, the PDFs of the N_2O-O_3 correlations are exemplary shown for 15 February 2009 as observed by the MLS instrument (top) and as derived from CLaMS simulations with and without smoothing by the averaging kernel (bottom). In contrast to MLS, original CLaMS output shows the polar correlation and that also disappears if the averaging kernel is applied to CLaMS output. This polar correlation can be attributed to some remnants of the polar vortex which are resolved by CLaMS. Within the model, the lifetime of the polar correlation is about three weeks longer compared to the last time this correlation was detected by the MLS instrument.

Thus, two question arise: are these small-scale structures resolved with CLaMS realistic and is the N_2O or rather the O_3-related coarse sampling of the MLS instrument that smoothes out the polar correlation of N_2O-O_3? To get an impression, how the averaging kernel smoothes out the modeled small scale filaments and tracer gradients, Fig. 13 shows the spatial distribution of N_2O vortex remnants on 20 February 2009 before and after applying the MLS averaging kernel procedure (right and left column, respectively). Here, N_2O distributions at two isentropic levels, 550 K (top row) and 650 K (bottom row) are shown, with black line denoting the strongly disturbed vortex edge.

ACPD
15, 4383–4426, 2015

Complementary, N_2O and O_3 profiles from the Atmospheric Chemistry Experiment (ACE) are used, which cross the potential surfaces θ = 550 and 660 K at this day (red circles as the profile positions at noon on each isentrope), as well as the corresponding CLaMS profiles before and after applying the averaging kernel. The nearest CLaMS APs are selected according to the same procedure as for the MLS data (see Sect. 3.2). Thus, the horizontal spatial distances of ACE profiles and corresponding CLaMS profiles are less than 50 km (1.5°). The vertical resolution of ACE profiles is about 3–4 km (Bernath et al., 2005; Boone et al., 2005).

It can be seen that the vertical variability of the untreated CLaMS simulation of N_2O is confirmed by the corresponding ACE profile (top panel in Fig. 14). On the other hand, this variability is removed from the CLaMS simulation if the MLS averaging kernel is applied and, consequently, the comparison with the ACE observations becomes worse. However, the smoothing does not significantly change the O_3 profiles (bottom panel in Fig. 14). This is mainly because the vertical variability of O_3 is much smaller if compared with the N_2O profile and not because of a higher vertical resolution of the MLS-based O_3 observations (i.e. 2.5–3 km for O_3 vs. 5–6 km for N_2O).

This can also be inferred from the comparison of the horizontal and vertical gradients of both tracers. Within the vertical range between θ = 400 and 800 K, the horizontal variability of N_2O across the vortex edge (~ 100 ppbv) is comparable with the vertical variability (~ 150 ppbv), whereas O_3 gradient across polar vortex edge (around 1 ~ 2 ppmv) is much smaller than its vertical gradient in stratosphere (~ 5 ppmv). Therefore, the filaments or vortex remnants which are not completely mixed, contribute to a more pronounced vertical variability of N_2O than of the O_3 profiles.

ACPD
15, 4383–4426, 2015

Acknowledgements. We thank ECMWF for providing reanalysis data and MLS team for providing the N_2O and O_3 data. Excellent programming support was provided by N. Thomas. We thank the Atmospheric Chemistry Experiment (ACE) team, a Canadian-led mission mainly supported by the Canadian Space Agency and the Natural Sciences and Engineering Research Council of Canada, for providing the N_2O and O_3 data.

The service charges for this open access publication have been covered by a Research Centre of the Helmholtz Association.

References

Andrews, D. G., Holton, J. R., and Leovy, C. B.: Middle Atmosphere Dynamics, Academic Press, San Diego, USA, 1987. 4384, 4388, 4389

Ayarzagüena, B., Langematz, U., and Serrano, E.: Tropospheric forcing of the stratosphere: a comparative study of the two different major stratospheric warmings in 2009 and 2010, J. Geophys. Res.-Atmos., 116, 2011. 4385

Bernath, P., McElroy, C., Abrams, M., Boone, C., Butler, M., Camy-Peyret, C., Carleer, M., Clerbaux, C., Coheur, P., Colin, R., DeCola, P., Bernath, P., McElroy, C., Abrams, M., Boone, C., Butler, M., Camy-Peyret, C., Carleer, M., Clerbaux, C., Coheur, P., Colin, R., DeCola, P., DeMaziere, M., Drummond, J., Dufour, D., Evans, W., Fast, H., Fussen, D., Gilbert, K., Jennings, D., Llewellyn, E., Lowe, R., Mahieu, E., McConnell, J., McHugh, M., McLeod, S., Michaud, R., Midwinter, C., Nassar, R., Nichitiu, F., Nowlan, C., Rinsland, C., Rochon, Y., Rowlands, N., Semeniuk, K., Simon, P., Skelton, R., Sloan, J., Soucy, M., Strong, K., Tremblay, P., Turnbull, D., Walker, K., Walkty, I., Wardle, D., Wehrle, V., Zander, R., and Zou, J.: Atmospheric Chemistry Experiment (ACE): mission overview, Geophys. Res. Lett., 32, doi:10.1029/2005GL022386, 2005. 4406

Boone, C. D., Nassar, R., Walker, K. A., Rochon, Y., McLeod, S. D., Rinsland, C. P., and Bernath, P. F.: Retrievals for the atmospheric chemistry experiment Fourier-transform spectrometer, Appl. Optics, 44, 7218–7231, 2005. 4406

Charlton, A. J. and Polvani, L. M.: A new look at stratospheric sudden warmings, Part I: climatology and modeling benchmarks, J. Climate, 20, 449–469, 2007. 4388

ACPD
15, 4383–4426, 2015

Crutzen, P. J., Grooß, J.-U., Brühl, C., Müller, R., and Russell III, J. M.: A Reevaluation of the ozone budget with HALOE UARS data: no evidence for the ozone deficit, Science, 268, 705–708, 1995. 4402

Dee, D. P., Uppala, S. M., Simmons, A. J., Berrisford, P., Poli, P., Kobayashi, S., Andrae, U., Balmaseda, M. A., Balsamo, G., Bauer, P., Bechtold, P., Beljaars, A. C. M., van de Berg, L., Bidlot, J., Bormann, N., Delsol, C., Dragani, R., Fuentes, M., Geer, A. J., Haimberger, L., Healy, S. B., Hersbach, H., Holm, E. V., Isaksen, L., Kallberg, P., Kohler, M., Matricardi, M., McNally, A. P., Monge-Sanz, B. M., Morcrette, J. J., Park, B. K., Peubey, C., de Rosnay, P., Tavolato, C., Thepaut, J. N., and Vitart, F.: The ERA-Interim reanalysis: configuration and performance of the data assimilation system, Q. J. Roy. Meteor. Soc., 137, 553–597, doi:10.1002/qj.828, 2011. 4386, 4389, 4391

Dickinson, R. E.: On the exact and approximate linear theory of vertically propagating planetary Rossby waves forced at a spherical lower boundary, Mon. Weather Rev., 96, 405–415, 1968. 4389

Edouard, S., Legras, B., Lefèvre, F., and Eymard, R.: The effect of small-scale inhomogeneities on ozone depletion in the Arctic, Nature, 384, 444–447, 1996. 4385

Eliassen, A.: Slow thermally or frictionally controlled meridional circulation in a circular vortex, Astrophysica Norvegica, 5, 19, 1951. 4385

Grooß, J.-U., Günther, G., Müller, R., Konopka, P., Bausch, S., Schlager, H., Voigt, C., Volk, C.M., and Toon, G. C.: Simulation of denitrification and ozone loss for the Arctic winter 2002/2003, Atmos. Chem. Phys., 5, 1437–1448, doi:10.5194/acp-5-1437-2005, 2005a. 4391

Grooß, J.-U., Konopka, P., and Müller, R.: Ozone chemistry during the 2002 Antarctic vortex split, J. Atmos. Sci., 62, 860–870, 2005b. 4385

Harada, Y., Goto, A., Hasegawa, H., Fujikawa, N., Naoe, H., and Hirooka, T.: A major stratospheric sudden warming event in January 2009, J. Atmos. Sci., 67, 2052–2069, 2010. 4385

Haynes, P. and Shuckburgh, E.: Effective diffusivity as a diagnostic of atmospheric transport, 1, Stratosphere, J. Geophys. Res., 105, 22777–22794, 2000. 4394

Hegglin, M. I. and Shepherd, T. G.: O_3-N_2O correlations from the Atmospheric Chemistry Experiment: revisiting a diagnostic of transport and chemistry in the stratosphere, J. Geophys. Res., D19301, doi:10.1029/2006JD008281, 2007. 4387

Holton, J. R., Haynes, P., McIntyre, M. E., Douglass, A. R., Rood, R. B., and Pfister, L.: Stratosphere-troposphere exchange, Rev. Geophys., 33, 403–439, 1995. 4393

ACPD
15, 4383–4426, 2015

Hoppe, C. M., Hoffmann, L., Konopka, P., Grooß, J.-U., Ploeger, F., Günther, G., Jöckel, P., and Müller, R.: The implementation of the CLaMS Lagrangian transport core into the chemistry climate model EMAC 2.40.1: application on age of air and transport of long-lived trace species, Geosci. Model Dev., 7, 2639–2651, doi:10.5194/gmd-7-2639-2014, 2014. 4386

Khosrawi, F., Grooß, J.-U., Müller, R., Konopka, P., Kouker, W., Ruhnke, R., Reddmann, T., and Riese, M.: Intercomparison between Lagrangian and Eulerian simulations of the development of mid-latitude streamers as observed by CRISTA, Atmos. Chem. Phys., 5, 85–95, doi:10.5194/acp-5-85-2005, 2005. 4390

Konopka, P., Grooß, J.-U., Bausch, S., Müller, R., McKenna, D. S., Morgenstern, O., and Orsolini, Y.: Dynamics and chemistry of vortex remnants in late Arctic spring 1997 and 2000: Simulations with the Chemical Lagrangian Model of the Stratosphere (CLaMS), Atmos. Chem. Phys., 3, 839–849, doi:10.5194/acp-3-839-2003, 2003. 4385

Konopka, P., Steinhorst, H.-M., Grooß, J.-U., Günther, G., Müller, R., Elkins, J. W., Jost, H.-J., Richard, E., Schmidt, U., Toon, G., and McKenna, D. S.: Mixing and ozone loss in the 1999–2000 Arctic vortex: simulations with the 3-dimensional Chemical Lagrangian Model of the Stratosphere (CLaMS), J. Geophys. Res., 109, D02315, doi:10.1029/2003JD003792, 2004. 4386, 4390, 4391

Konopka, P., Grooß, J.-U., Hoppel, K. W., Steinhorst, H.-M., and Müller, R.: Mixing and chemical ozone loss during and after the Antarctic polar vortex major warming in September 2002, J. Atmos. Sci., 62, 848–859, 2005. 4385

Konopka, P., Günther, G., Müller, R., dos Santos, F. H. S., Schiller, C., Ravegnani, F., Ulanovsky, A., Schlager, H., Volk, C. M., Viciani, S., Pan, L. L., McKenna, D.-S., and Riese, M.: Contribution of mixing to upward transport across the tropical tropopause layer (TTL), Atmos. Chem. Phys., 7, 3285–3308, doi:10.5194/acp-7-3285-2007, 2007. 4386

Kuttippurath, J. and Nikulin, G.: A comparative study of the major sudden stratospheric warmings in the Arctic winters 2003/2004–2009/2010, Atmos. Chem. Phys., 12, 8115–8129, doi:10.5194/acp-12-8115-2012, 2012. 4386, 4402

Labitzke, K. and Kunze, M.: On the remarkable Arctic winter in 2008/2009, J. Geophys. Res.-Atmos., 114, D00I02, doi:10.1029/2009JD012273, 2009. 4385

Livesey, N. J., Read, W. G., Froidevaux, L., Lambert, A., Manney, G. L., Pumphrey, H. C., Santee, M. L., Schwartz, M. J., Wang, S., Cofield, R. E., Cuddy, D. T., Fuller, R. A., Jarnot, R. F., Jiang, J. H., Knosp, B. W., Stek, P. C., Wagner, P. A., and Wu, D. L.: Version 3.3 Level 2 data quality and description document, JPL D-33509, 2011. 4391, 4392

ACPD
15, 4383–4426, 2015

Livesey, N. J., Logan, J. A., Santee, M. L., Waters, J. W., Doherty, R. M., Read, W. G., Froidevaux, L., and Jiang, J. H.: Interrelated variations of O_3, CO and deep convection in the tropical/subtropical upper troposphere observed by the Aura Microwave Limb Sounder (MLS) during 2004–2011, Atmos. Chem. Phys., 13, 579–598, doi:10.5194/acp-13-579-2013, 2013. 4392

Manney, G. L., Krüger, K., Sabutis, J. L., Amina Sena, S., and Pawson, S.: The remarkable 2003–2004 winter and other recent warm winters in the Arctic stratosphere in the late 1990s, J. Geophys. Res., 110, D04107, doi:10.1029/2004JD005367, 2005. 4385

Manney, G. L., Krüger, K., Pawson, S., Minschwaner, K., Schwartz, M. J., Daffer, W. H., Livesey, N. J., Mlynczak, M. G., Remsberg, E. E., Russell, J. M., and Water, J. W.: The evolution of the stratopause during the 2006 major warming: satellite data and assimilated meteorological analyses, J. Geophys. Res.-Atmos., 113, 2008. 4385

Manney, G. L., Schwartz, M. J., Krüger, K., Santee, M. L., Pawson, S., Lee, J. N., Daffer, W. H., Fuller, R. A., and Livesey, N. J.: Aura Microwave Limb Sounder observations of dynamics and transport during the record-breaking 2009 Arctic stratospheric major warming, Geophys. Res. Lett., 36, L12815, doi:10.1029/2009GL038586, 2009. 4385

Matsuno, T.: A dynamical model of the stratospheric sudden warming, J. Atmos. Sci., 28, 1479–1494, 1971. 4384, 4389

McIntyre, M. E., and Palmer, T. N.: Breaking planetary waves in the stratosphere, Nature, 305, 593–600, 1983. 4385, 4386, 4393

McKenna, D. S., Grooß, J.-U., Günther, G., Konopka, P., Müller, R., Carver, G., and Sasano, Y.: A new Chemical Lagrangian Model of the Stratosphere (CLaMS): 2. Formulation of chemistry scheme and initialization, J. Geophys. Res., 107, 4256, doi:10.1029/2000JD000113, 2002a. 4391

McKenna, D. S., Konopka, P., Grooß, J.-U., Günther, G., Müller, R., Spang, R., Offermann, D., and Orsolini, Y.: A new Chemical Lagrangian Model of the Stratosphere (CLaMS): 1. Formulation of advection and mixing, J. Geophys. Res., 107, 4309, doi:10.1029/2000JD000114, 2002b. 4386, 4390

McInturff, R.: Stratospheric warmings: synoptic, dynamic and general-circulation aspects, NASA Ref. Pub., 1017, 174, 1978. 4388

Mlynczak, M. G., Mertens, C. J., Garcia, R. R., and Portmann, R. W.: A detailed evaluation of the stratospheric heat budget: 2. Global radiation balance and diabatic circulations, J. Geophys. Res.-Atmos., 104, 6039–6066, 1999. 4390

ACPD
15, 4383–4426, 2015

Müller, R., Crutzen, P. J., Grooß, J.-U., Brühl, C., Russell III, J. M., and Tuck, A. F.: Chlorine activation and ozone depletion in the Arctic vortex: observations by the Halogen Occultation Experiment on the Upper Atmosphere Research Satellite, J. Geophys. Res., 101, 12531–12554, 1996. 4387

Müller, R., Schmidt, U., Engel, A., McKenna, D. S., and Proffitt, M. H.: The O_3-N_2O relationship from balloon-borne observations as a measure of Arctic ozone loss in 1991/92, Q. J. Roy. Meteor. Soc., 127, 1389–1412, 2001. 4387

Nash, E. R., Newman, P. A., Rosenfield, J. E., and Schoeberl, M. R.: An objective determination of the polar vortex using Ertel's potential vorticity, J. Geophys. Res., 101, 9471–9478, 1996. 4393, 4417

Newman, P. A., Nash, E. R., and Rosenfield, J. E.: What controls the temperature of the Arctic stratosphere during the spring?, J. Geophys. Res., 106, 19999–20010, doi:10.1029/2000JD000061, 2001. 4389

Orsolini, Y. J., Hansen, G., Hoppe, U. P., Manney, G. L., and Fricke, K. H.: Dynamical modelling of wintertime lidar observations in the Arctic, Q. J. Roy. Meteor. Soc., 123, 785–800, 1997. 4385

Ploeger, F., Konopka, P., Günther, G., Grooß, J.-U., and Müller, R.: Impact of the vertical velocity scheme on modeling transport across the tropical tropopause layer, J. Geophys. Res., 115, doi:10.1029/2009JD012023, 2010. 4386, 4391

Ploeger, F., Günther, G., Konopka, P., Fueglistaler, S., Müller, R., Hoppe, C., Kunz, A., Spang, R., Grooß, J.-U., and Riese, M.: Horizontal water vapor transport in the lower stratosphere from subtropics to high latitudes during boreal summer, J. Geophys. Res., 118, 8111–8127, doi:10.1002/jgrd.50636, 2013. 4392

Plumb, R. A.: A "tropical pipe" model of stratospheric transport, J. Geophys. Res., 101, 3957–3972, 1996. 4386, 4387, 4393

Plumb, R. A.: Tracer interrelationships in the stratosphere, Rev. Geophys., 45, RG4005, doi:10.1029/2005RG000179, 2007. 4387, 4397, 4401

Plumb, R. A. and Bell, R. C.: A model of the quasi-biennial oscillation on an equatorial beta-plane, Q. J. Roy. Meteor. Soc., 108, 335–352, 1982. 4385

Polvani, L. M., Waugh, D., and Plumb, R. A.: On the subtropical edge of the stratospheric surf zone, J. Atmos. Sci., 52, 1288–1309, 1995. 4394

Pommrich, R., Müller, R., Grooß, J.-U., Konopka, P., Ploeger, F., Vogel, B., Tao, M., Hoppe, C. M., Günther, G., Spelten, N., Hoffmann, L., Pumphrey, H.-C., Viciani, S.,

ACPD
15, 4383–4426, 2015

D'Amato, F., Volk, C. M., Hoor, P., Schlager, H., and Riese, M.: Tropical troposphere to stratosphere transport of carbon monoxide and long-lived trace species in the Chemical Lagrangian Model of the Stratosphere (CLaMS), Geosci. Model Dev., 7, 2895–2916, doi:10.5194/gmd-7-2895-2014, 2014. 4391

Punge, H. J., Konopka, P., Giorgetta, M. A., and Müller, R.: Effects of the quasi-biennial oscillation on low-latitude transport in the stratosphere derived from trajectory calculations, J. Geophys. Res., 114, D03102, doi:10.1029/2008JD010518, 2009. 4394

Randel, W. J., Garcia, R. R., and Wu, F.: Time-dependent upwelling in the tropical lower stratosphere estimated from the zonal-mean momentum budget, J. Atmos. Sci., 59, 2141–2152, 2002. 4388

Riese, M., Ploeger, F., Rap, A., Vogel, B., Konopka, P., Dameris, M., and Forster, P. M.: Impact of uncertainties in atmospheric mixing on simulated UTLS composition and related radiative effects, J. Geophys. Res., 117, D16, doi:10.1029/2012JD017751, 2012. 4386

Shuckburgh, E., Norton, W., Iwi, A., and Haynes, P.: Influence of the quasi-biennial oscillation on isentropic transport and mixing in the tropics and subtropics, J. Geophys. Res.-Atmos., 106, 14327–14337, 2001. 4394

Sofieva, V. F., Kalakoski, N., Verronen, P. T., Päivärinta, S.-M., Kyrölä, E., Backman, L., and Tamminen, J.: Polar-night O_3, NO_2 and NO_3 distributions during sudden stratospheric warmings in 2003–2008 as seen by GOMOS/Envisat, Atmos. Chem. Phys., 12, 1051–1066, doi:10.5194/acp-12-1051-2012, 2012. 4386

Steinhorst, H.-M., Konopka, P., Günther, G., and Müller, R.: How permeable is the edge of the Arctic vortex – Model studies of the winter 1999–2000, J. Geophys. Res., 110, D06105, doi:10.1029/2004JD005268, 2005. 4386

Tuck, A. F.: Depletion of Antarctic ozone, Nature, 321, 729–730, 1986. 4385, 4386

Volk, C. M., Elkins, J. W., Fahey, D. W., Salawitch, R. J., Dutton, G. S., Gilligan, J. M., Proffitt, M. H., Loewenstein, M., Podolske, J. R., Minschwaner, K., Margitan, J. J., and Chan, K. R.: Quantifying transport between the tropical and mid-latitude lower stratosphere, Science, 272, 1763–1768, 1996. 4387

ACPD
15, 4383–4426, 2015

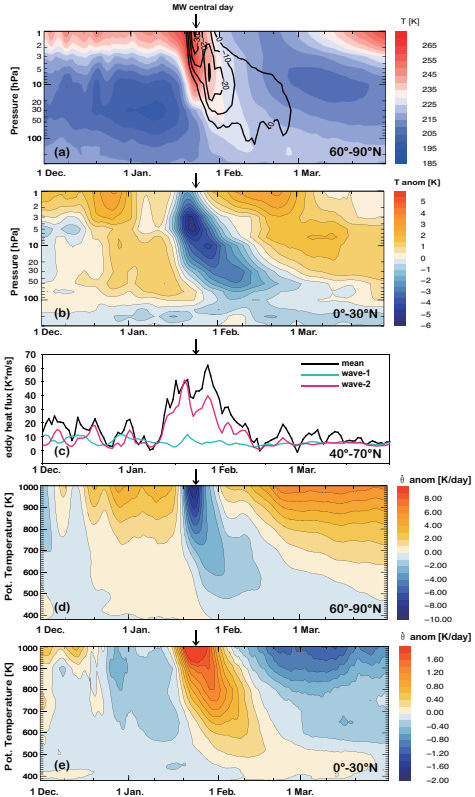

Figure 1. (a) Polar cap area weighted mean temperature (60–90° N) overlaid with zonal mean easterlies at 60° N (black contours in $m\,s^{-1}$), **(b)** tropical zonal mean temperature anomaly from the 24 year mean of ERA-Interim reanalysis(0–20° N), **(c)** eddy heat flux (40–70° N, black) on 100 hPa and its decomposition into wave-1 (blue) and wave-2 (red) components, **(d)** polar mean (60–90° N) anomaly of the heating rates from the 24 year mean of ERA-Interim reanalysis $Q = d\theta/dt = \dot{\theta}$ (for more details see next section), **(e)** same as **(d)** but for 0–30° N.

ACPD
15, 4383–4426, 2015

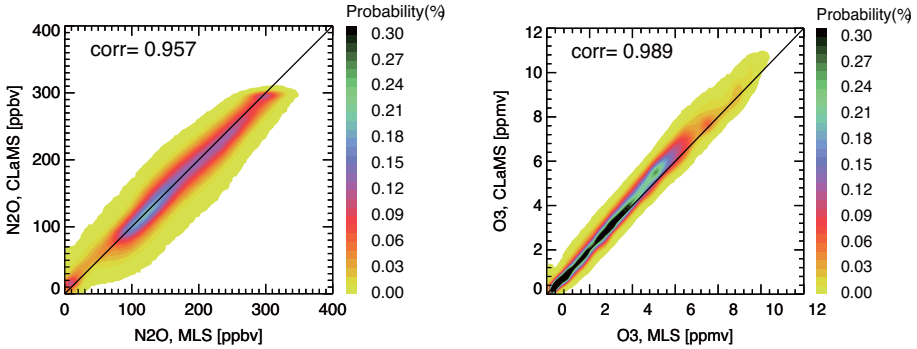

Figure 2. PDFs of MLS observations and CLaMS reference simulation from 1 December 2008 to 1 April 2009 for APs in the Northern Hemisphere with 400 K < θ < 1000 K (left: N_2O, right: O_3).

ACPD
15, 4383–4426, 2015

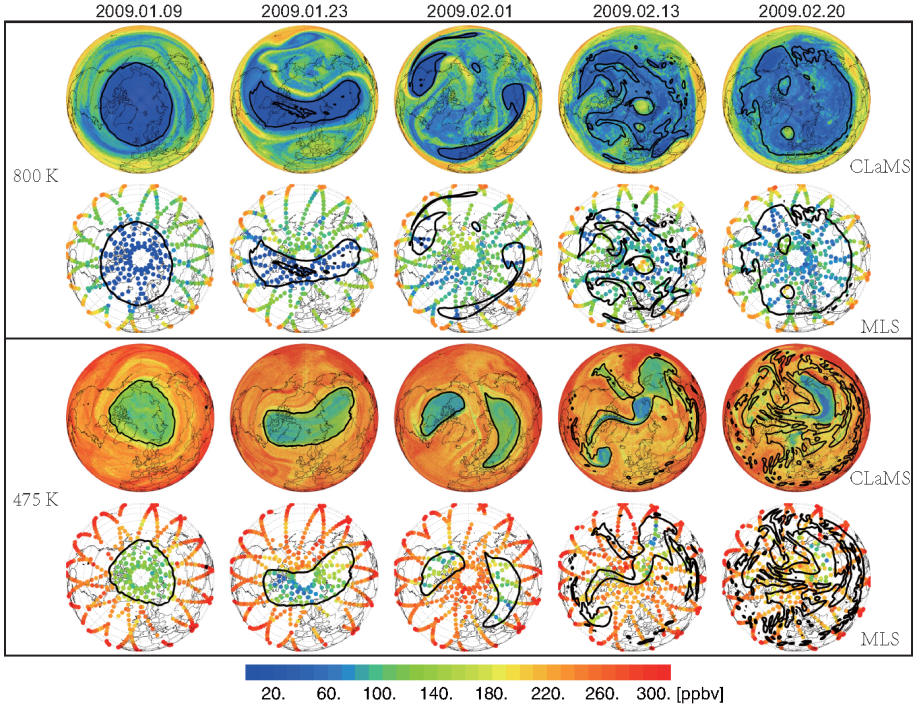

Figure 3. N_2O distribution at $\theta = 800$ K (top 2 rows) and 475 K (bottom 2 rows) interpolated from CLaMS simulation and MLS observations for five selected days in 2009 before and after the MW event. The black contours show the edge of the polar vortex.

ACPD
15, 4383–4426, 2015

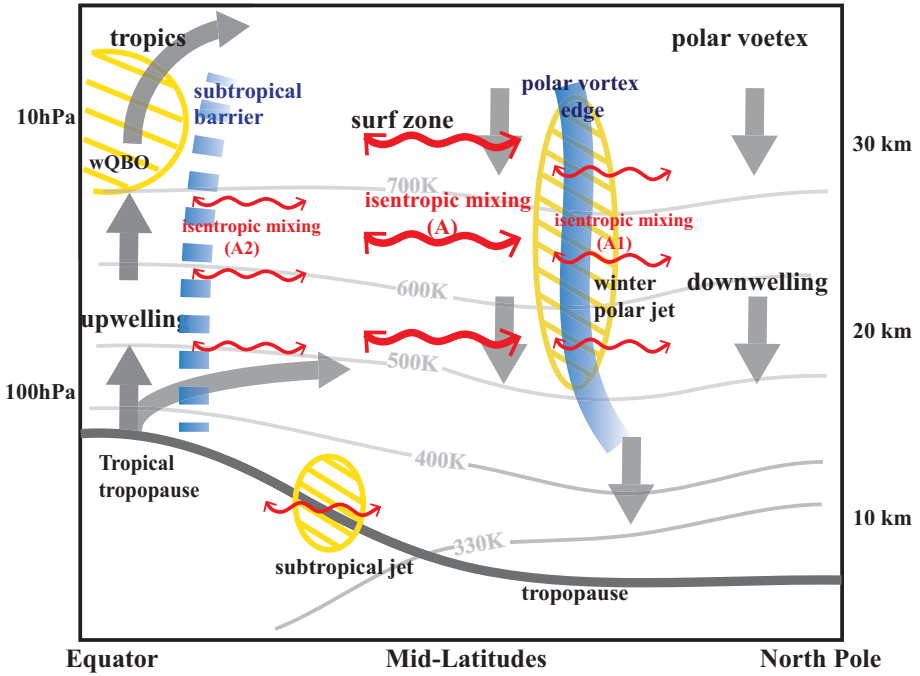

Figure 4. Schematic picture of transport and mixing processes in the winter stratosphere. The thick blue lines show the barriers, the gray arrows indicate the direction of the BD circulation. Yellow shaded areas stand for strong westerlies. Red two-headed arrows indicate isentropic mixing, with thicker and thinner arrows showing stronger mixing in the surf zone and weaker mixing across the transport barriers, respectively. For a better overview, the tropopause with the subtropical jet are also marked.

ACPD
15, 4383–4426, 2015

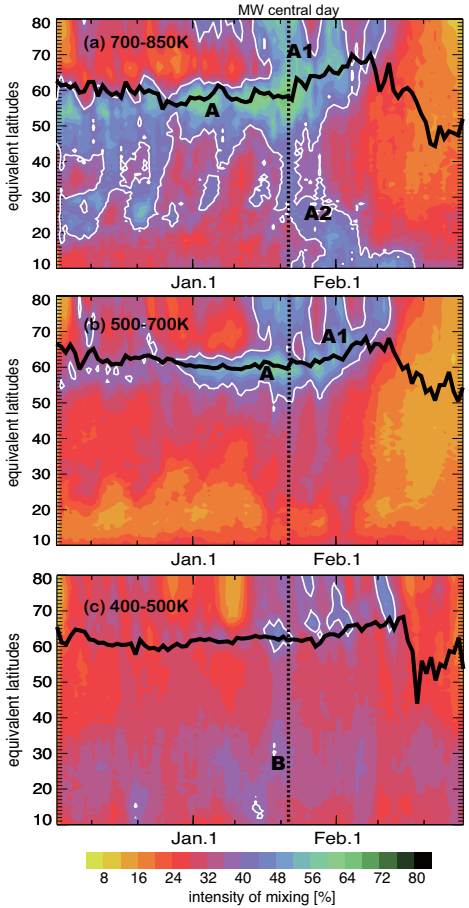

Figure 5. CLaMS zonal mean mixing intensity within 3 layers: **(a)** 700–850 K, **(b)** 500–700 K, **(c)** 400–500 K overlaid by the location of the vortex edge (thick black lines, Nash et al., 1996) and the white contours indicate the mixing intensity of 40 %.

ACPD
15, 4383–4426, 2015

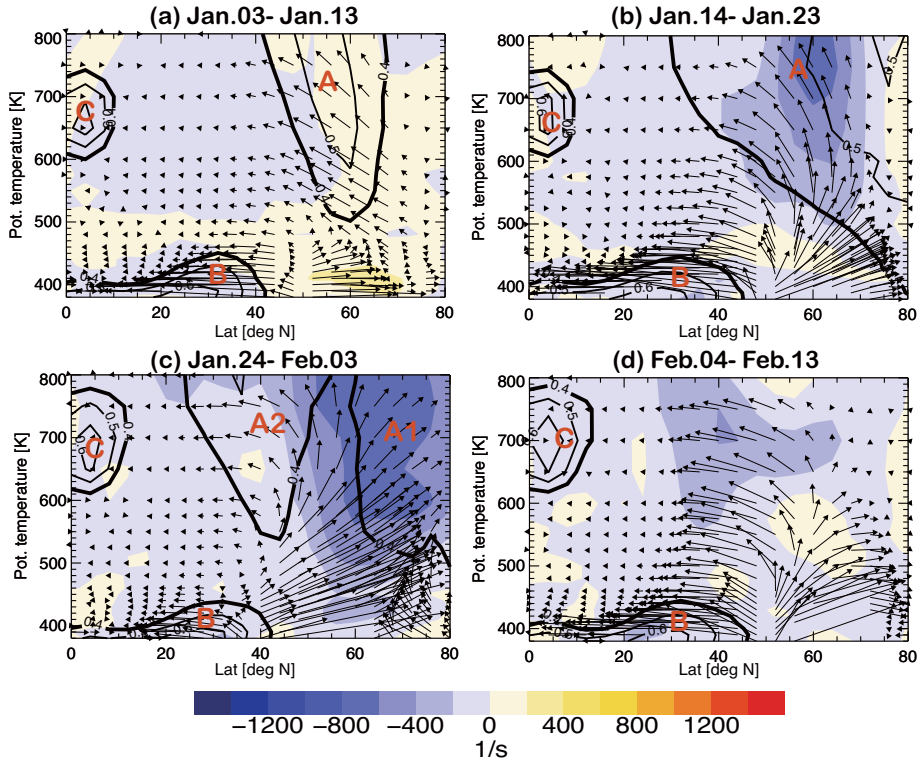

Figure 6. EP flux (arrows) and its divergence (colored bluish). Black contours indicate the mixing intensity larger than 0.4. The panels **(a–d)** show mean values averaged over 4 time periods: **(a)** 3–13 January, **(b)** 14–23 January, **(c)** 24 January–3 February, **(d)** 4–13 February.

ACPD
15, 4383–4426, 2015

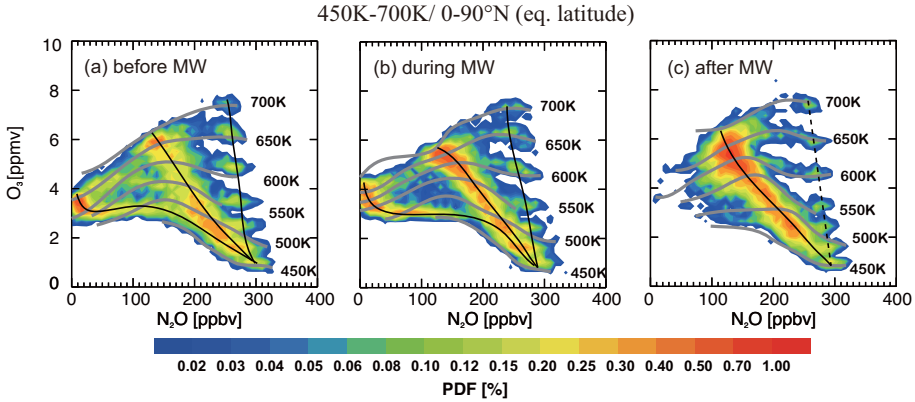

Figure 7. Correlation between N_2O and O_3 from the MLS observations within eq. latitudes 0–90° N and potential temperature range between 450 and 700 K shown as a PDF for 3 periods: **(a)** 18–28 December, **(b)** 18–28 January, **(c)** 18–28 February. The gray lines mark the isentropes (450, 500, 550, 600, 650, and 700 K).

ACPD
15, 4383–4426, 2015

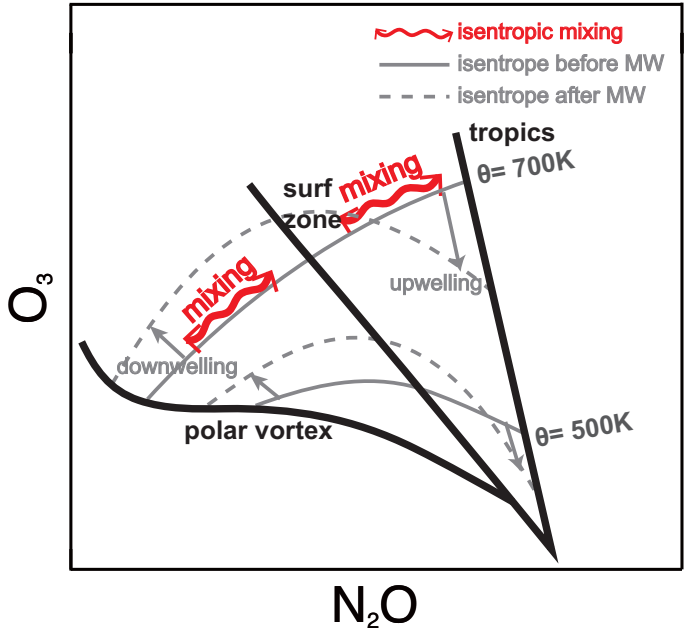

Figure 8. Schematic diagram of the N_2O-O_3 correlations (solid black lines) observed before and after the MW in 2009. Red arrows indicate the effect of isentropic mixing. Gray lines denote the isentropic levels before (solid) and after (dashed) the MW. The change of the position of a prescribed point in the N_2O-O_3 space relative to these isentropes describes the effect of an idealized (mixing-free) cross-isentropic motion (up- or downwelling).

ACPD
15, 4383–4426, 2015

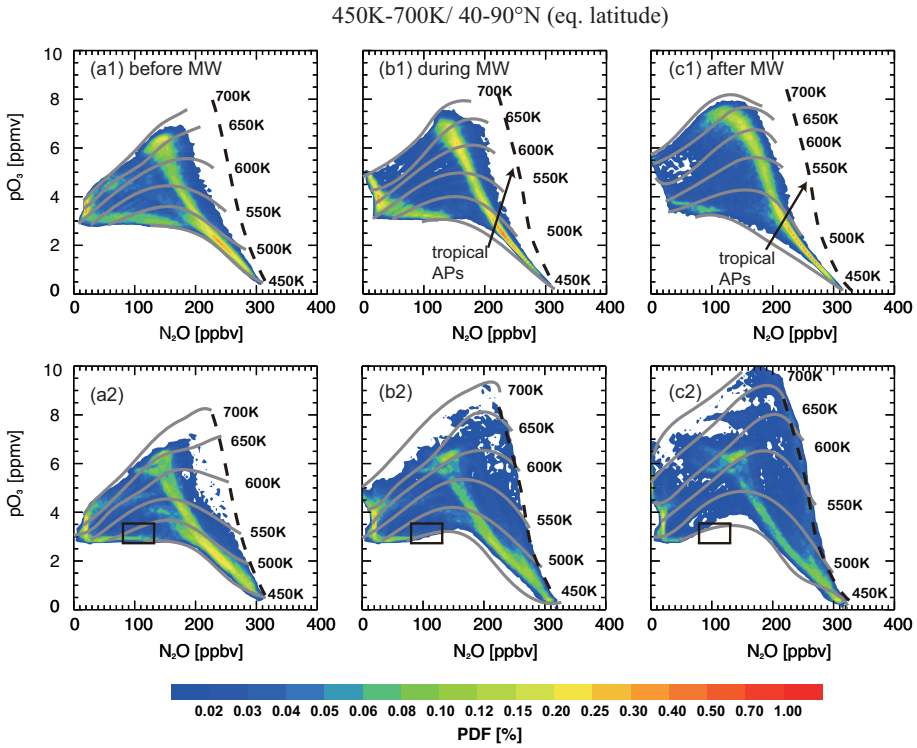

Figure 9. Effect of mixing on the N_2O-pO_3 correlations for the same 3 time periods as in Fig. 7 (from **a** to **c**). Top and bottom rows show CLaMS with and without mixing, respectively. The shown PDFs are calculated from the APs with the potential temperature between 450 and 700 K and with eq. latitudes between 40 and 90° N.

ACPD
15, 4383–4426, 2015

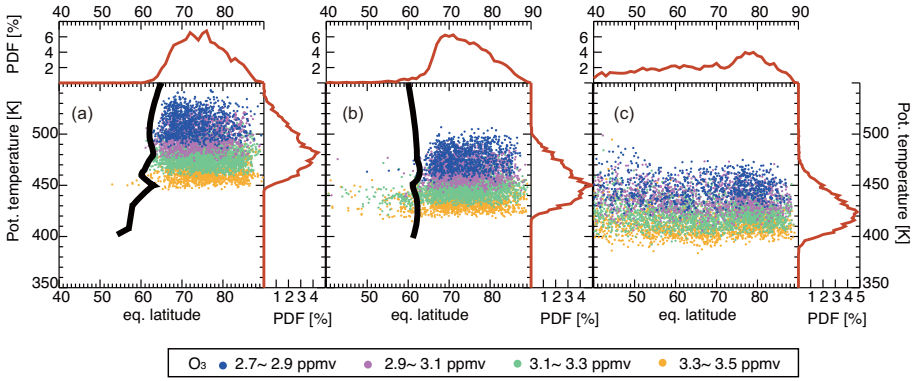

Figure 10. Spatial distribution in the eq. latitude-θ space of the APs defined by the mixing ratios of N_2O and pO_3 inside the square in Fig. 9a2, i.e with N_2O and pO_3 values from 80 to 130 ppbv and from 2.7 to 3.5 ppmv, respectively, calculated from CLaMS run without mixing. **(a)** 23 December 2008; **(b)** 23 January 2009; **(c)** 23 February 2009. Colors indicate different ranges of pO_3 values. The PDFs along the eq. latitude and potential temperature axes are shown as red lines. Thick black lines denotes the edge of the polar vortex.

ACPD
15, 4383–4426, 2015

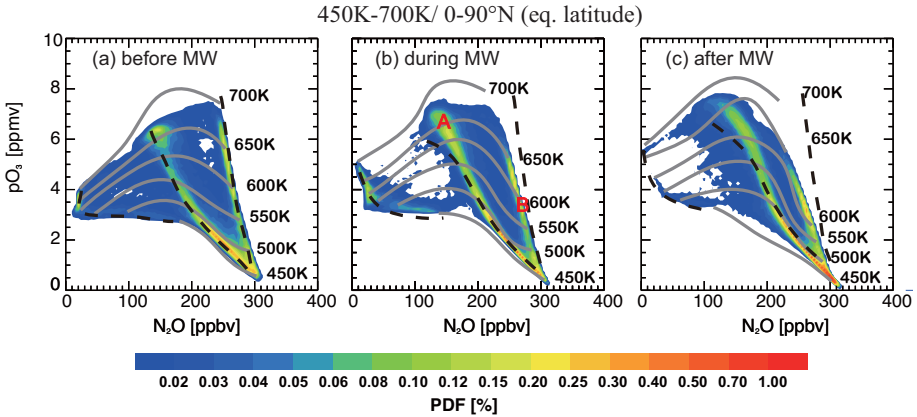

Figure 11. Impact of O_3-chemistry on the temporal evolution of the N_2O-O_3 correlations. The PDFs are calculated from the N_2O-pO_3 correlations of APs with eq. latitudes 0–90° N and potential temperatures 450–700 K. The considered time periods are the same as in Fig. 7. The dashed black curves fit the maxima of the N_2O-O_3 correlations (PDFs) derived from a CLaMS run with a full stratospheric ozone chemistry.

ACPD
15, 4383–4426, 2015

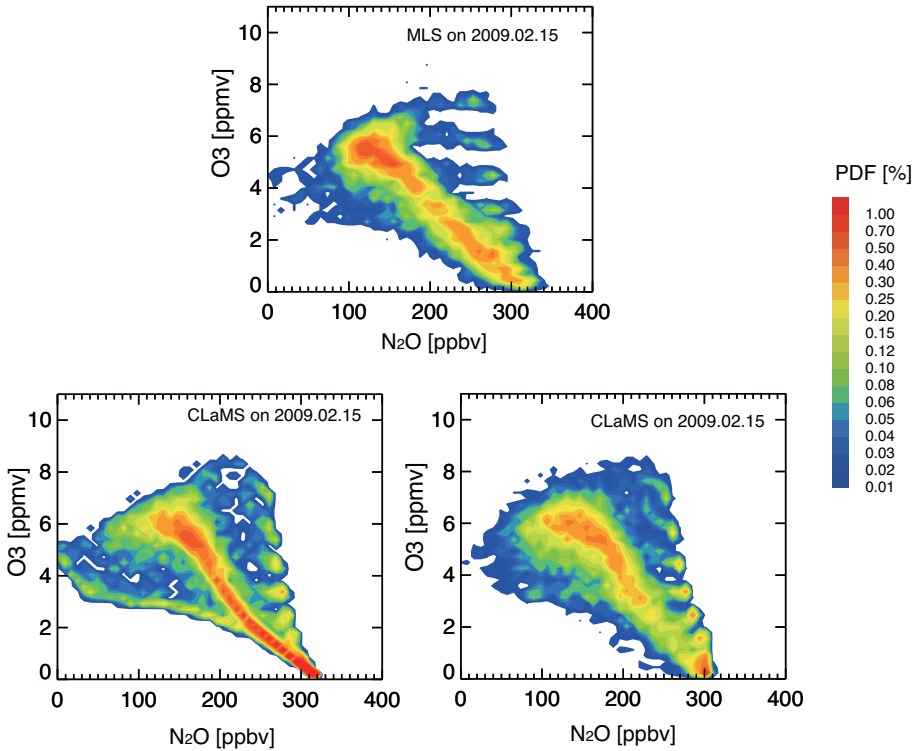

Figure 12. PDFs of N_2O-O_3 correlations on 15 February 2009 from MLS observations (top); from the reference CLaMS simulation without applying the averaging kernel (bottom left) and after applying the averaging kernel (bottom right).

ACPD
15, 4383–4426, 2015

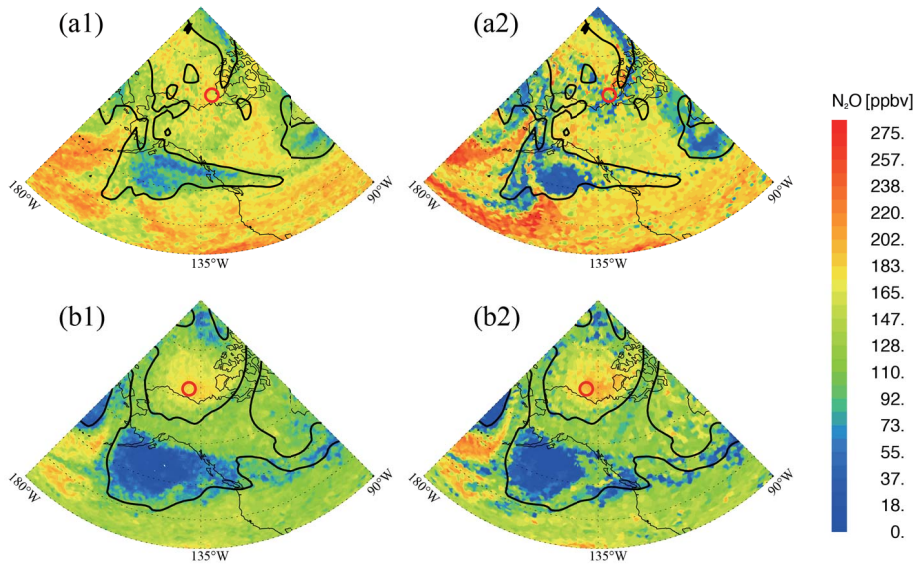

Figure 13. Spatial distribution of N_2O on 20 February 2009, i.e., almost 1 month after the MW at θ = 550 K (top row) and 650 K (bottom row). Here the results of the reference run with and without the averaging kernel are shown in the left and right column, respectively. Black line is vortex edge, the red circles are the noon-footprints calculated by the observed ACE profile through back and forward trajectory.

ACPD
15, 4383–4426, 2015

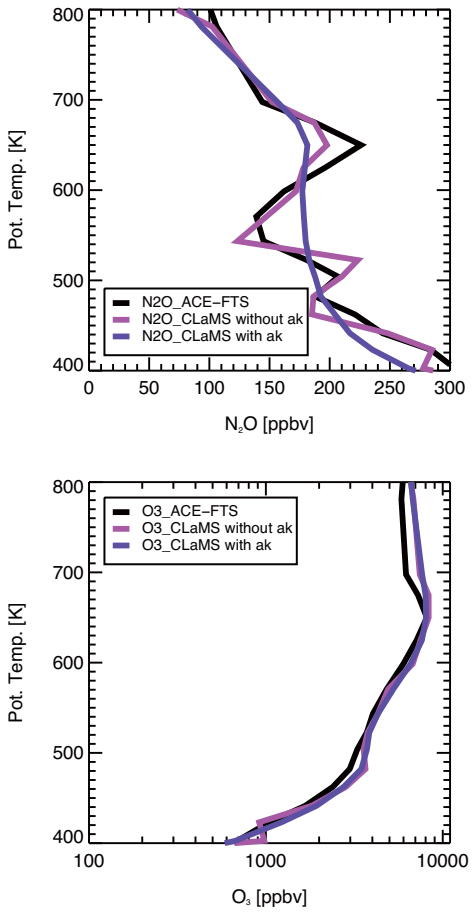

Figure 14. N_2O (top) and O_3 (bottom) profiles of ACE observations (black) on 20 February located at 73.05° N, 137.11° W at 30 km and of corresponding CLaMS simulation before (blue) and after (purple) applying the MLS averaging kernel.

ACPD
15, 4383–4426, 2015